Research Article

ADVANCED PHOTONICS NEXUS

# Vectorial optomechanical sensing: controlling coherent coupling in an engineered fiber resonator

**Heng Wang,[a] Lin Ma,[a,b] Chao Song,[a,b] Qin Nie,[a] Xuehao Hu,[c] Xiaoli Li,[d,e] Kun Xiao,[b] Rui Min,[d,e] and Zhuo Wang[b,*]**
[a]Shenyang Aerospace University, College of Science, Shenyang, China
[b]Beijing Normal University, Faculty of Arts and Sciences, Department of Physics, Zhuhai, China
[c]University of Mons, Department of Electromagnetism and Telecommunication, Mons, Belgium
[d]Beijing Normal University, Faculty of Arts and Sciences, Department of Psychology, Zhuhai, China
[e]Beijing Normal University, Faculty of Psychology, Beijing, China

**Abstract.** In precision optomechanical sensing, polarization instability is typically regarded as a fundamental noise source that must be suppressed, posing a basic limitation to the conventional sensing paradigm. This work extends this paradigm by demonstrating the active control and coherent utilization of polarization as a distinct sensing channel for signal enhancement. We introduce "vectorial optomechanical sensing," the approach that transforms this polarization "noise" into a valuable signal. This is achieved using an engineered planar dual-spiral optical fiber resonator that deterministically partitions a single mechanical strain into two orthogonal modes: frequency and polarization. A crucial control experiment directly validates the engineered nature of this effect, showing a strong, tunable polarization dependence that is absent in conventional single-loop designs. A nonideal physical model incorporating a minor phase offset excellently describes the experimental data, revealing a realistic sensitivity enhancement of over 188%. The optimized sensor achieves a sensitivity of 557.82 mV/Pa, a signal-to-noise ratio of 24.8 dB, and a noise-equivalent pressure of 2.45 mPa/$\sqrt{\text{Hz}}$. Notably, we demonstrate a sensing bandwidth extending to 3 kHz under Pound–Drever–Hall (PDH) interrogation, overcoming the conventional low-frequency limitation of such resonant systems. Its high-fidelity signal capture capability is demonstrated by monitoring ballistocardiogram (BCG) signals with gold-standard validation and achieving high-accuracy classification of human speech. This principle of engineering coherent interplay between orthogonal modes offers a universal pathway for surpassing the conventional performance limits of diverse high-*Q* resonant systems.

Keywords: optomechanical sensing; vectorial sensing; polarization control; fiber optic resonator; high-*Q* resonator; biophysical monitoring; ballistocardiogram; noise transformation.

Received Nov. 10, 2025; revised manuscript received Jan. 7, 2026; accepted for publication Mar. 3, 2026; published online Mar. 31, 2026.



[DOI: 10.1117/1.APN.5.3.036009]

## 1 Introduction

The noninvasive monitoring and detailed analysis of human physiological processes are cornerstones of modern healthcare and biomedical research.[1,2] Although macroscopic parameters are routinely measured, a deeper understanding often lies hidden within subtle biomechanical signatures—the faint, yet information-rich vibrations and acoustic emissions generated by the body's intricate workings. These signatures range from the fine temporal details of the ballistocardiogram (BCG), which reflect cardiovascular dynamics,[3,4] and micro-tremors indicative of neurological conditions, to the nuanced harmonic content in vocal cord vibrations, which reveals laryngeal health and serves as a vocal biomarker for disease diagnosis.[5] Capturing these signals with high fidelity offers a powerful window into physiological function and pathological deviations, often preceding

*Address all correspondence to Zhuo Wang, zhuowang@bnu.edu.cn

clinically apparent symptoms. Consequently, technologies capable of accessing and precisely interpreting these subtle mechanical cues hold transformative potential for early diagnosis, continuous health monitoring, and more intuitive human-machine interfaces.

Despite this potential, the reliable detection and analysis of these biological vibrations remain a significant technological hurdle. These signals are inherently challenging: they often exhibit extremely low amplitudes (sometimes pico- to nanometer-scale displacements or sub-Pascal pressure levels), possess complex, nonlinear characteristics, and are invariably corrupted by significant physiological and environmental noise. Conventional sensors, such as micro-electro-mechanical system (MEMS) accelerometers or piezoelectric elements commonly used in wearable devices, often face performance limitations in sensitivity, are susceptible to electrical interference, and can suffer from long-term stability issues.[6,7] Furthermore, they may lack the necessary bandwidth or dynamic range to capture the full complexity of the signals without distortion, particularly at high frequencies where MEMS sensors can introduce erroneous data. Critically, beyond mere detection, there is a pressing need for sensing modalities that can effectively encode the high-dimensional dynamic information contained within these signals to enable sophisticated downstream analysis.

To overcome these limitations, optical sensing methodologies,[8] particularly those based on high quality ($Q$) factor optical resonators, have garnered significant interest.[9,10] High-$Q$ resonators are exceptionally promising, as their sharp resonance features—a direct consequence of long photon lifetimes within the cavity—are exquisitely sensitive to minute external perturbations.[9,11] Among these, optical fiber resonators provide distinct advantages for biomedical applications, including inherent flexibility for conformal contact and intrinsic immunity to electromagnetic interference.[12] To date, such resonant sensors have almost exclusively operated on a single-channel principle, transducing mechanical strain into a resonant frequency shift. In this paradigm, polarization instability—a well-known issue in resonant fiber optic systems—is ubiquitously treated as a detrimental noise source that must be rigorously suppressed to ensure measurement stability and precision. It is worth noting that such polarization-related effects have been extensively studied in the context of fiber optic gyroscopes (FOGs) and polarization-maintaining fiber (PMF) optics.[13–16] However, in those traditional domains, stress-induced polarization cross-coupling is typically stochastic—arising from random environmental perturbations—and is treated as "parasitic noise" that must be rigorously suppressed to maintain scalar accuracy. In stark contrast, our work represents a fundamental reversal of this logic. Instead of suppressing polarization effects, we introduce a deterministic symmetry-breaking mechanism via the "planar dual-spiral" architecture to actively engineer the polarization cross-coupling. By transforming this physical phenomenon from a random noise source into a controllable sensing degree of freedom, we establish a paradigm of vectorial optomechanical sensing, where the vector nature of light is harvested to coherently enhance the signal rather than degrade it.

This conventional viewpoint, however, overlooks a significant opportunity. Although the individual effects of strain on frequency and polarization are understood physical phenomena, the systematic engineering and active control of the coherent interplay between these two orthogonal modes within a single high-$Q$ resonator remains an unexplored area. This leads to a key physical question: Can we transform this cross-coupling, typically regarded as random noise, into a deterministic physical resource for signal enhancement that can be precisely controlled by an external parameter? This work provides an affirmative answer to this question. We introduce "vectorial optomechanical sensing," a paradigm distinct from conventional scalar sensing. We define this term not by the multiplicity of output channels, but by the active exploitation of the optical vector degree of freedom—polarization—during the fundamental transduction process. Unlike traditional methods, where strain is mapped solely onto a scalar frequency shift while polarization effects are suppressed as noise, our approach utilizes an engineered resonator to deterministically partition the mechanical input into orthogonal frequency (scalar) and polarization (vector) modes. These modes are then coherently superposed to enhance the final signal. This strategy is realized using an innovative planar dual-spiral fiber resonator, whose architecture is engineered to synchronously and efficiently partition a single mechanical vibration into the two orthogonal optical channels. We establish a complete theoretical framework showing how these two channels coherently superimpose within a Pound–Drever–Hall (PDH) system.[17,18] As core evidence, this theory is then decisively validated by a novel experimental paradigm based on a controllable polarization bias. Finally, the power of this mechanism is demonstrated by applying the sensor to the high-fidelity monitoring of complex physiological signals, proving its significant potential.

## 2 Theoretical Framework and Physical Model

### 2.1 Concept and Structural Principle of Coherent Dual-Channel Optomechanical Transduction

The central challenge in precision biophysical sensing, as outlined in the introduction, is the development of novel paradigms capable of transducing faint mechanical vibrations into high-fidelity optical signals. To overcome the sensitivity limitations of conventional single-channel sensors, this work explores a novel concept: leveraging multiple orthogonal degrees of freedom of light for coherent signal detection. The potential of this approach is to significantly enhance the signal gain beyond conventional limits. However, the realization of such a "multichannel" sensing scheme hinges on a critical challenge: a physical structure must be designed to act as a "mode converter." This structure must be capable of taking a single, macroscopic mechanical strain and synchronously and controllably partitioning it onto these orthogonal optical channels.

The proposed device represents a structural variation of the optical fiber ring resonator that fully exploits the flexibility of the fiber cavity as a mechanical transducer. By reconfiguring the conventional circular cavity into a planar dual-spiral geometry, the resonator not only retains its high optical quality factor but also gains the ability to respond anisotropically to external mechanical stimuli. Specifically, the sensor employs a planar Archimedean dual-spiral geometry constructed from a standard polarization-maintaining fiber. The retention of the soft polymer coating ensures mechanical robustness and flexibility during the intricate winding process. The structure is engineered to maximize the sensing interaction length—achieving a total effective fiber length of 46 cm—while being compactly integrated within the 43 mm diameter active area of the silicone diaphragm.

Crucially, the spiral winding geometry is optimized to satisfy the adiabatic bending condition, ensuring that the bending radius throughout the structure exceeds the critical threshold to preserve the resonator's high $Q$-factor ($10^7$). The selection of this dual-spiral topology—as opposed to a conventional single-loop or concentric circular coil—is governed by the principle of symmetry breaking. In a standard single-loop geometry, the structural rotational symmetry leads to an isotropic stress distribution ($\sigma_r \approx \sigma_\theta$) within the fiber cross-section under uniform diaphragm deformation, producing negligible photoelastic birefringence. In contrast, the dual-spiral structure introduces a deterministic geometric anisotropy. The spiral trajectory creates a continuously varying angle between the fiber axis and the diaphragm's radial stress field, ensuring that the stress components transverse to the fiber core are nondegenerate ($\sigma_x \neq \sigma_y$). This mechanism efficiently "opens" the polarization channel by inducing a strain-dependent linear birefringence via the elasto-optic effect, which is the physical foundation of our vectorial sensing paradigm. As illustrated in Fig. 1, when a single mechanical strain $\epsilon(t)$ acts on this structure, it no longer solely causes a resonant frequency shift $\delta\omega(t)$ in the conventional sense (the frequency channel). Instead, it synchronously induces a dynamic polarization state rotation $\Delta\theta(t)$ (the polarization channel). The final output signal is a coherent superposition of these two orthogonal channel signals, and its total sensitivity $S_{\text{total}}$ can be actively tuned by an externally controllable static polarization bias angle, $\theta_0$. It is important to clarify the physical nature of the "vectorial" mechanism in our single-readout architecture. Although the final signal retrieved by the PDH system is a scalar intensity value, it represents the coherent projection of the vector polarization mode onto the scalar frequency mode. By manipulating the external static polarization bias angle $\theta_0$, we actively control this projection efficiency. Therefore, the system operates as a vector-based transducer with a scalar readout, where the sensitivity enhancement is derived from the controlled interference between the excited orthogonal degrees of freedom. This figure establishes a complete and self-consistent theoretical and structural foundation for the analysis of all experimental results in the subsequent sections.

### 2.2 Mechanical Response Model of the System: The Driven Damped Harmonic Oscillator

To profoundly reveal the underlying physical principles of the ultra-high sensitivity achieved by the planar dual-spiral optical resonator biophysical sensor in this work, this section establishes a complete end-to-end theoretical model, from the external mechanical excitation to the final electrical output. This model demonstrates that the exceptional performance of the sensor originates from an unprecedented dynamic frequency-polarization coupling enhancement mechanism. The core of this mechanism is that the designed sensing structure can synchronously partition a single mechanical strain into the orthogonal frequency and polarization degrees of freedom of light, which are then coherently demodulated by a PDH system to achieve a tunable signal gain.

The mechanical front end of the sensor, which consists of the diaphragm and the attached spiral fiber composite structure, can be accurately modeled as a driven damped harmonic oscillator (DDHO). This model provides the physical basis for describing the system's frequency response characteristics and defining its operational bandwidth. When an external dynamic pressure signal $P(\omega)$ acts upon the diaphragm, the system generates a dynamic base strain $\varepsilon(\omega)$. Their relationship is described by a transfer function $H_{P\epsilon}(\omega)$:

$$\varepsilon(\omega) = H_{P\epsilon}(\omega) \cdot P(\omega) = [K_{P\epsilon} \cdot H_{\text{norm}}(\omega)] \cdot P(\omega), \quad (1)$$

where $K_{P\epsilon}$ is the static pressure-to-strain conversion coefficient of the system (unit: strain/Pa), representing the fundamental mechanical sensitivity at low frequencies. $H_{\text{norm}}(\omega)$ is the normalized frequency response function determined by the DDHO

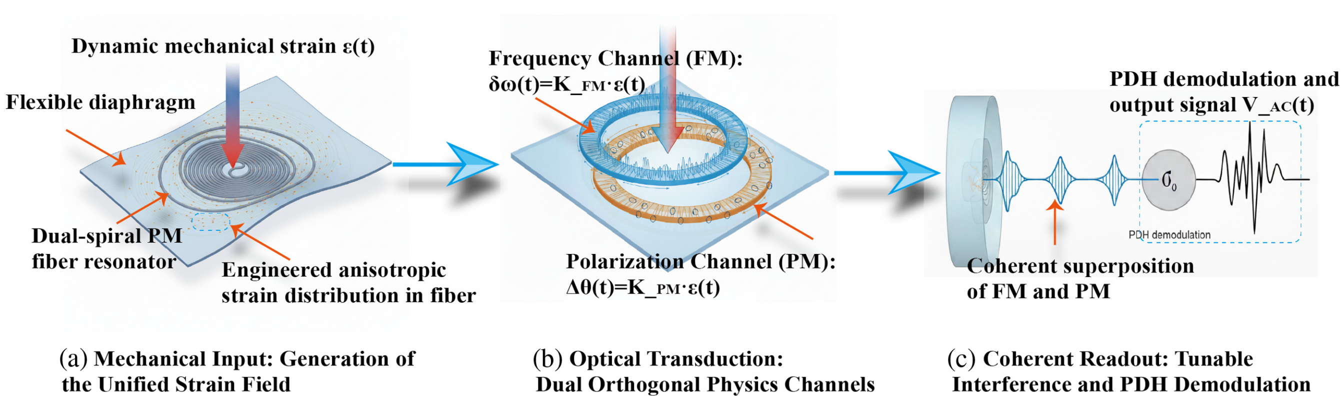


**Fig. 1** Coherent dual-channel optomechanical transduction in a planar dual-spiral fiber resonator. (a) Mechanical actuation—A single dynamic strain $\varepsilon(t)$ applied to the flexible diaphragm generates an engineered anisotropic stress field in the dual-spiral polarization-maintaining fiber (PMF). (b) Dual optical transduction—the same strain simultaneously induces two orthogonal optical effects: an isotropic elongation producing a frequency shift $\delta\omega(t) = K_{\text{FM}}\varepsilon(t)$ (blue channel) and an anisotropic compression causing polarization rotation $\Delta\theta(t) = K_{\text{PM}}\varepsilon(t)$ (orange channel). (c) Coherent readout—the frequency modulation (FM) and polarization modulation (PM) channels coherently recombine and are demodulated via the PDH scheme, yielding an enhanced output $V_{\text{AC}}(t) \propto [K_{\text{FM}} \cos\theta_0 + K_{\text{PM}} \sin\theta_0]\varepsilon(t)$. Together, the sequence illustrates "one mechanical input → two orthogonal optical channels → one coherent output."

characteristics, where $\omega$ is the angular frequency of the signal. By designing the natural mechanical resonant frequency $\omega_0$ to be much higher than the target operational frequency band, a flat response ($|H_{\mathrm{norm}}(\omega)| \approx 1$) within the bandwidth is ensured, thus enabling distortion-free signal detection. The base strain $\varepsilon(\omega)$ generated from Eq. (1) is the root cause that drives all subsequent optical effects. The core innovation of this work lies in the ability of the planar dual-spiral resonator to synchronously induce two orthogonal optical modulations from this strain, which are then coherently demodulated by the PDH system.

#### 2.2.1 Frequency modulation (FM channel)

The strain $\varepsilon(t)$ causes an isotropic change in the optical path length, leading to a linear shift $\delta\omega(t)$ in the resonant frequency $\omega_c$:

$$\delta\omega(t) = K_{\mathrm{FM}} \cdot \varepsilon(t). \tag{2}$$

#### 2.2.2 Polarization modulation (PM channel)

The anisotropic stress field induced by the strain $\varepsilon(t)$ creates a dynamic birefringence, which leads to a small rotation $\Delta\theta(t)$ in the polarization state of the reflected light:.

$$\Delta\theta(t) = K_{\mathrm{PM}} \cdot \varepsilon(t). \tag{3}$$

The core of the PDH technique is the measurement of the beat note at frequency $\Omega_m$ on the photodetector, which arises from the interference of the reflected carrier $E_c(t)$ and sidebands $E_{\pm 1}(t)$. After passing through a fixed analyzer, the effective field amplitudes are approximately:

- $E_c(t) \approx A_c(\delta\omega(t)) \cdot \cos(\theta_0 + \Delta\theta(t))$
- $E_{\pm 1}(t) \approx A_{sb}$ (The sidebands are promptly reflected, and their amplitude and polarization are considered constant)

where $A_c(\delta\omega(t))$ is the frequency-detuning-dependent carrier amplitude, and $\theta(t) = \theta_0 + \Delta\theta(t)$ is the total polarization angle. The photocurrent component at $\Omega_m$, $I_{\Omega_m}(t)$, is proportional to the interference term. The amplitude of this beat note, $A_{\mathrm{beat}}(t)$, can be expressed as

$$A_{\mathrm{beat}}(t) \propto A_c(\delta\omega(t)) \cdot \cos(\theta_0 + \Delta\theta(t)). \tag{4}$$

Equation (4) shows that the beat note amplitude is modulated by two independent physical quantities: the frequency detuning (via $A_c$) and the polarization rotation (via $\cos(\theta)$). We now perform a first-order Taylor expansion on both perturbation terms:

- **Frequency Term:** $A_c(\delta\omega(t)) \approx A_{c0} + k_1 \cdot \delta\omega(t)$, where $A_{c0}$ is the static operating point amplitude and $k_1$ is the first-order response coefficient.
- **Polarization Term:** $\cos(\theta_0 + \Delta\theta(t)) \approx \cos(\theta_0) - \sin(\theta_0) \cdot \Delta\theta(t)$.

Substituting both linear expressions into Eq. (4):

$$A_{\mathrm{beat}}(t) \propto [A_{c0} + k_1 \cdot \delta\omega(t)] \cdot [\cos(\theta_0) - \sin(\theta_0) \cdot \Delta\theta(t)].$$

Expanding this product gives:

$$A_{\mathrm{beat}}(t) \propto A_{c0} \cos(\theta_0) + k_1 \cos(\theta_0) \cdot \delta\omega(t) - A_{c0} \sin(\theta_0) \cdot \Delta\theta(t) - k_1 \sin(\theta_0) \cdot \delta\omega(t)\Delta\theta(t).$$

The final AC sensing signal demodulated by the PDH system, $V_{\mathrm{AC}}(t)$, is proportional to all first-order terms synchronous with the target signal $\varepsilon(t)$. The DC term is filtered out, and the cross-term $\delta\omega(t)\Delta\theta(t)$ is neglected (as the product of two small dynamic perturbations, it is vanishingly small compared with the dominant first-order linear terms), yielding the final AC signal expression:

$$V_{\mathrm{AC}}(t) \propto k_1 \cos(\theta_0) \cdot \delta\omega(t) - A_{c0} \sin(\theta_0) \cdot \Delta\theta(t). \tag{5}$$

This rigorously proves from first principles that the total output signal is a linear superposition of two parallel, independent first-order terms.

Based on Eq. (5), the total AC signal can be written as

$$V_{\mathrm{AC}}(t) \propto \cos(\theta_0) \cdot \delta\omega(t) + \sin(\theta_0) \cdot \Delta\theta(t). \tag{6}$$

Substituting Eqs. (2) and (3) into Eq. (6) using the strain $\varepsilon(t)$ as the unified input yields:

$$V_{\mathrm{AC}}(t) \propto [K_{\mathrm{FM}} \cos(\theta_0) + K_{\mathrm{PM}} \sin(\theta_0)] \cdot \varepsilon(t). \tag{7}$$

The total sensitivity of the sensor, $S_{\mathrm{total}}$, is defined as the ratio of the output voltage to the input strain. This leads to the final total sensitivity equation:

$$S_{\mathrm{total}}(\theta_0) = S_{\mathrm{FM}} \cdot \cos(\theta_0) + S_{\mathrm{PM}} \cdot \sin(\theta_0), \tag{8}$$

where $S_{\mathrm{FM}}$ and $S_{\mathrm{PM}}$ are the intrinsic strain-to-voltage sensitivity constants for the frequency and polarization channels, respectively. This equation quantitatively predicts the system's behavior and reveals the mechanism for signal gain. The total sensitivity is a coherent superposition of the signals from the two orthogonal channels. By tuning the external bias angle $\theta_0$, the interference can be actively controlled. When the intrinsic sensitivity of the polarization channel, $S_{\mathrm{PM}}$, is significantly larger than that of the frequency channel, $S_{\mathrm{FM}}$, a coherent signal gain far exceeding that of a conventional single-channel sensor can be achieved by choosing an optimal bias angle, $\theta_{0,\max} = \arctan(S_{\mathrm{PM}}/S_{\mathrm{FM}})$.

## 3 Experimental Validation of Coherent Dual-Channel Optomechanical Transduction

### 3.1 Experimental Configuration and Measurement Scheme

To address the significant challenge of capturing faint biophysical dynamics with high fidelity in precision health monitoring, a biophysical sensing system based on a high-$Q$ optical resonator was proposed and constructed. Figure 2 systematically illustrates the core concept of this system, its key structural innovation, and the novel physical model that governs its operation. The core concept of the sensor involves the noninvasive capture of subtle mechanical vibrations originating from internal physiological processes, achieved through a flexible sensing head in conformal contact with the human body [Fig. 2(a)]. The entire system is built upon a PDH precision interrogation architecture, designed to transduce minute mechanical deformations into high signal-to-noise ratio (SNR) electrical signals. The key to realizing this goal lies in the design of the sensing head. Figure 2(b) presents the central structural innovation of this work: a planar dual-spiral resonator. Unlike conventional

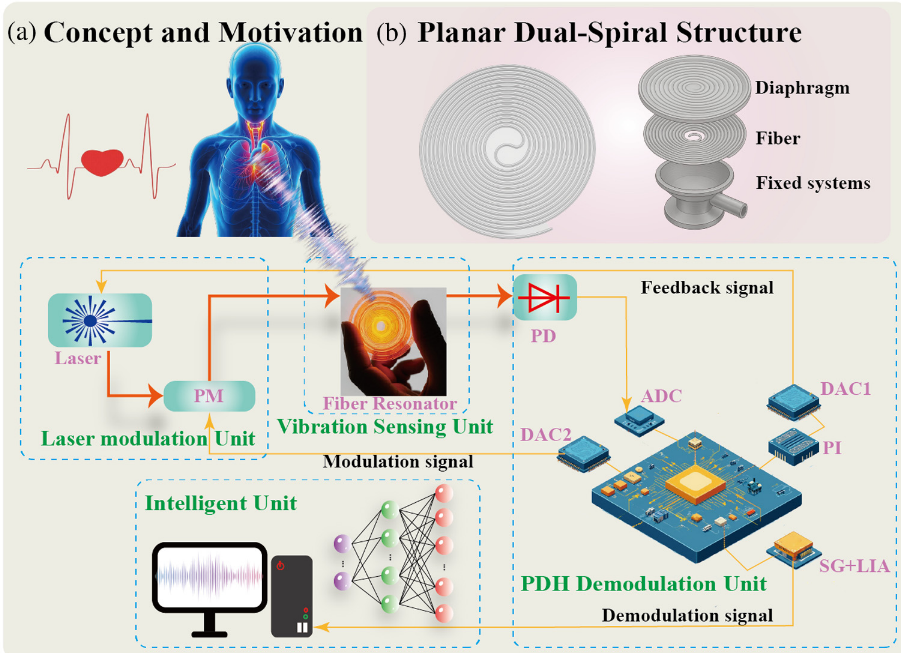


**Fig. 2** Concept, device architecture, and core physical model of the multichannel coherent enhancement sensor. (a) Conceptual illustration of the proposed noninvasive biophysical sensing. The sensor maintains conformal contact with human skin to capture subtle mechanical vibrations (e.g., BCG and speech signals), which are demodulated by a system based on a PDH precision locking scheme. (b) The core innovative device architecture: the planar dual-spiral resonator. It is designed to actively engineer a dynamic anisotropic strain field by precisely arranging a polarization-maintaining fiber in a counter-wound pattern on a flexible diaphragm.

single-loop configurations, this design involves a unique counter-wound pattern, where a polarization-maintaining fiber is precisely fixed onto a flexible diaphragm. This structure is not merely a geometric arrangement; we propose that its physical purpose is to actively engineer a dynamic anisotropic strain field. This special strain field is considered the prerequisite for the novel physical mechanism proposed herein. The validity of this core hypothesis will be directly verified by the key experimental results that follow.

### 3.2 Experimental Verification of Tunable Coupling and Sensitivity Enhancement

The fabricated optical fiber planar dual-spiral resonator consists of a 46 cm polarization-maintaining fiber precisely arranged in the designed planar dual-spiral pattern onto a 43 mm diameter, 350 $\mu$m thick medical-grade silicone diaphragm and secured using UV adhesive. This planar dual-spiral structure uses a sophisticated counter-wound process to maximize the sensor's symmetry and offset environmental perturbations. The specific preparation method starts from the precise center point of the entire optical fiber: half of the fiber length is coiled clockwise along the designed spiral path from the inside out; then, the other half of the fiber is covered in a counter-clockwise direction along the exact same geometric path, winding back from the outside in. This counter-wound geometry is specifically designed such that the bending of the diaphragm induces differential tension and shear stress between the clockwise and counter-clockwise spirals. This generates a net dynamic anisotropic stress field, in stark contrast to the predominantly isotropic strain experienced by a simple circular loop.

Subsequently, we mounted the integrated optomechanical structure onto a standard stethoscope head cavity, demonstrating the feasibility of our design and its potential application compatibility, bridging the gap between the concept (Fig. 1) and physical implementation, and connecting the resonator to the system in Fig. 1(b). To accurately evaluate the dynamic performance of the sensing unit, we built a standardized vibration test platform. The test platform uses a loudspeaker driven by a function generator as a vibration source to generate a calibrated sound pressure level, which is measured by a sound level meter placed near the sensor diaphragm. The absolute acoustic pressure P (in Pascals) acting on the diaphragm was derived from the measured sound pressure level ($L_p$, in dB) using the standard relation: $P = P_{\mathrm{ref}} \cdot 10^{(L_p/20)}$, where $P_{\mathrm{ref}} = 20\ \mu\mathrm{Pa}$ is the reference sound pressure in air.

A core premise of our work is that the planar dual-spiral geometry is specifically engineered to generate a dynamic anisotropic strain field, which is essential for activating the polarization channel. To provide direct evidence for this claim and to distinguish this engineered effect from any incidental anisotropy, we performed a crucial control experiment. We compared the polarization-dependent sensitivity of our dual-spiral sensor against that of a conventional single-loop resonator fabricated with identical materials and fiber length. To perform the polarization-dependent sensitivity measurements presented in Fig. 3, a manual fiber polarization controller was integrated into the optical path of the PDH system, immediately before the resonator. This controller allows the linearly polarized state of the

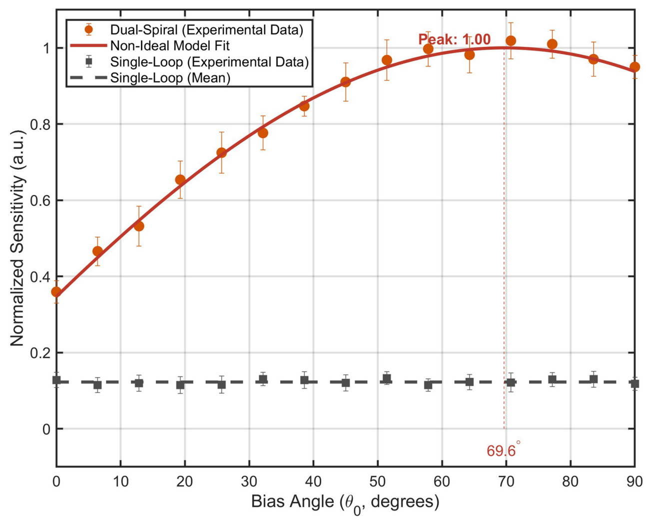


**Fig. 3** Control experiment validation for the engineered anisotropy mechanism. Comparison of the normalized sensitivity as a function of the static polarization bias angle for the planar dual-spiral sensor (orange data points) and a conventional single-loop resonator (gray data points) under identical experimental conditions. The dual-spiral sensor exhibits a strong, deterministic dependence that is excellently fitted by a nonideal coherent superposition model (solid red line). By contrast, the sensitivity of the single-loop resonator remains largely independent of the angle, showing only minor fluctuations around its mean value (dashed gray line). This comparison provides direct experimental proof for the core premise that the dual-spiral geometry is key to generating the engineered anisotropic response.

input laser to be rotated to any desired orientation by precisely applying stress and bends to the fiber. During the experiment, a fixed acoustic pressure at 1 kHz was first applied. The polarization controller was then systematically and incrementally rotated. At each step, the signal amplitude demodulated by the lock-in amplifier was recorded. By defining the initial state where the frequency channel's contribution is maximized and the polarization channel's contribution is minimized as the bias angle $\theta_0 = 0°$, we were able to calibrate the full functional relationship between the total sensitivity and the bias angle. The results of this comparative experiment are presented in Fig. 3, and the difference is stark and unambiguous. For the dual-spiral sensor (orange circles), the sensitivity exhibits a strong, deterministic dependence on the static polarization bias angle, which is excellently fitted by our nonideal coherent superposition model (solid red line). This demonstrates the presence of a powerful, well-defined polarization channel.

In stark contrast, the sensitivity of the conventional single-loop sensor (gray squares) shows only minor, random fluctuations around a constant mean value (dashed gray line), with no discernible dependence on the polarization angle. This direct, side-by-side comparison provides powerful experimental proof that it is the specific geometry of the dual-spiral structure, and not incidental effects, which is responsible for efficiently generating the anisotropic response. This result elevates the central premise of our work from a well-founded hypothesis to a physically verified principle. Having thus established the origin of the polarization channel, we proceed to analyze its effect on the sensor's overall performance. It is important to address the discrepancy between the observed enhancement of ∼188% and the >700% gain predicted by an idealized theoretical model. This difference does not stem from an experimental flaw but rather reveals a subtle, nonideal physical effect within the system. The primary reason for this is a minor phase offset (∼12° in our fit) between the two sensing channels. This small phase offset likely originates from the viscoelastic nature of the polymer diaphragm and adhesive. The development of the anisotropic stress field (polarization channel) may exhibit a slight phase lag relative to the isotropic optical path length change (frequency channel), a common characteristic in polymer-based mechanical systems. Although a full rheological characterization is beyond the scope of this work, this physically plausible mechanism accounts for the observed deviation from the ideal model. In an ideal case with perfect orthogonality, the baseline sensitivity at $\theta_0 = 0°$ would originate solely from the frequency channel. However, the presence of a phase offset causes a "leakage" from the much stronger polarization channel at this starting point, significantly elevating the baseline sensitivity. According to the enhancement formula, $(\text{Peak} - \text{Baseline})/\text{Baseline}$, a higher baseline value mathematically results in a lower calculated relative gain. Therefore, the 188% enhancement is a more rigorous and realistic assessment of the performance gain, precisely because our nonideal model accurately captures the physical details of the real-world system.

### *3.3 Performance Characterization and Comparative Benchmarking*

Having established the theoretical basis and design principles, we proceeded with the fabrication and experimental validation of the proposed optical biophysical sensing unit. Figure 4 presents the key characterization results and performance metrics, providing crucial experimental evidence supporting our core innovations. It should be noted that all sensor performance metrics reported in this section were characterized within a professional anechoic chamber under constant temperature conditions. These controlled conditions were intended to eliminate interference from ambient environmental noise and thermal drift, allowing for the precise characterization of the intrinsic performance limits of the sensor platform itself.

Leveraging this coherent enhancement mechanism validated in the previous section, we set the static polarization bias angle to its optimal value to characterize the sensor's peak performance and benchmark it against other technologies. The optical $Q$-factor of the designed optical fiber planar dual-spiral resonator was first characterized to achieve high-sensitivity detection of faint physiological vibration signals. The measured transmission spectrum [Fig. 4(a)] exhibits a sharp resonance dip, and a Lorentzian fit yields an intrinsic $Q$-factor exceeding $10^7$. This high $Q$-factor, corresponding to a narrow spectral linewidth, establishes a solid optical foundation for achieving high SNR sensing, which is essential for resolving subtle biological cues. The frequency response characteristic of the sensor is presented in the lower panel of Fig. 4(b). The sensor exhibits an effective and relatively flat response across a broad frequency range extending from 0.1 Hz to 3 kHz (tested under a 90.0 dB sound pressure level input). It is worth noting that achieving such a broadband response (up to 3 kHz) using a PDH interrogation scheme represents a significant advancement over conventional resonant sensors, which are often limited to static or quasi-static regimes. This bandwidth comprehensively covers the primary

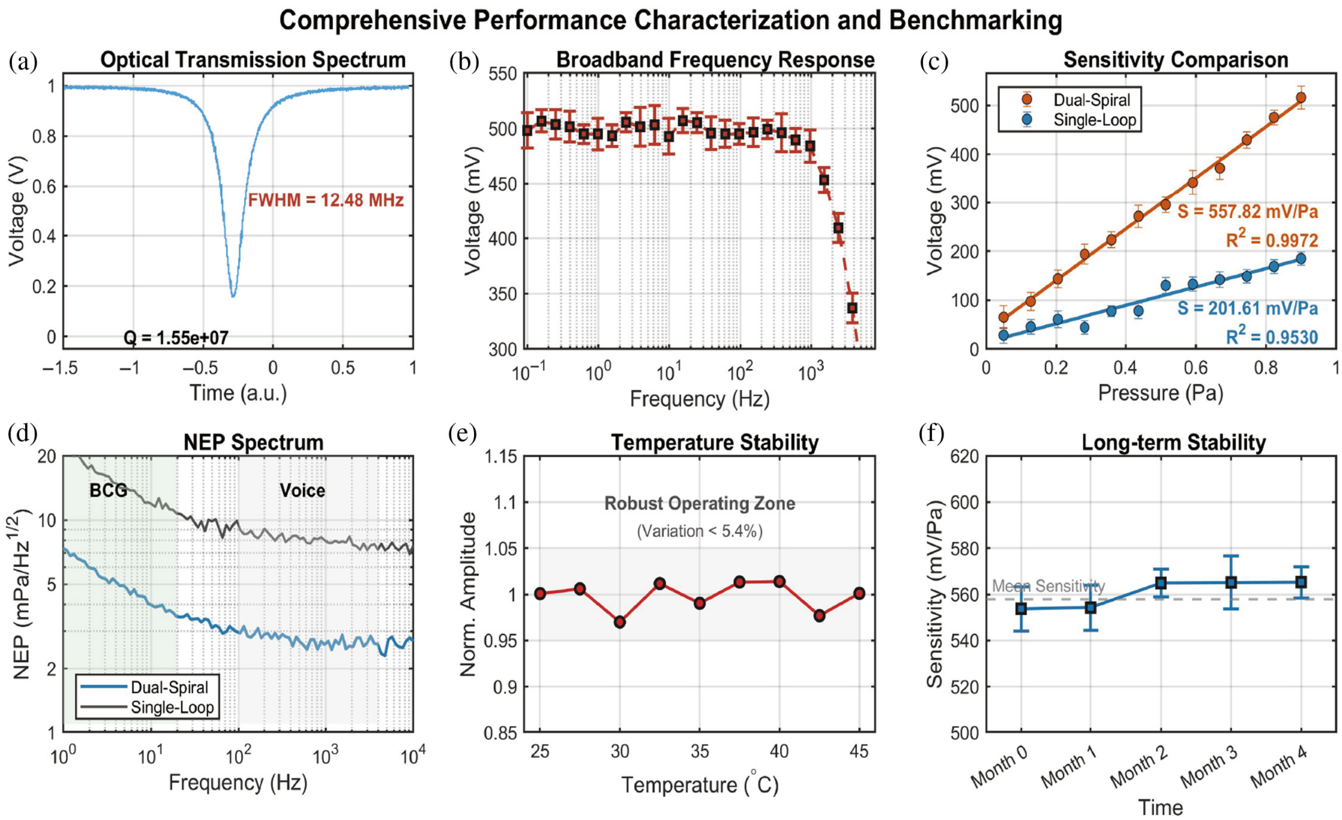


**Fig. 4** Comprehensive performance characterization and benchmarking of the sensor. (a) The optical transmission spectrum of the sensor, with a Lorentzian fit indicating a *Q* factor exceeding $10^7$. (b) The broadband frequency response of the sensor is from 0.1 Hz to 3 kHz. The inset shows a photograph of the experimental setup for performance characterization inside an anechoic chamber. (c) Sensitivity comparison between the dual-spiral resonator (red) and a conventional single-loop resonator (blue), verifying the significant gain from the coherent enhancement mechanism. (d) The noise equivalent pressure (NEP) spectrum of the sensor, showing a white-noise floor as low as 2.45 mPa/Hz at 1 kHz. (e) Temperature stability test results showing the normalized signal amplitude variation (<5.4%) over a temperature range of 25°C to 45°C. (f) Long-term stability analysis tracking the sensor's sensitivity over a 4-month period, demonstrating high consistency with a variation of <2.5%.

frequency ranges of targeted physiological signals, including the low-frequency components of BCG and the main spectral content of human voice signals. Particularly noteworthy is the excellent response maintained even at very low frequencies (down to 0.1 Hz), which is crucial for capturing quasi-static or slowly varying physiological processes often missed by sensors with higher low-frequency cutoffs. To directly validate the advantages conferred by our proposed planar dual-spiral structure design and the underpinning optomechanical gradient coupling enhancement, rigorous comparative tests were performed against a conventional single-loop optical fiber resonator sensing unit, as shown in Figs. 4(c) and 4(d). The baseline sensor was fabricated using the identical optical fiber length and diaphragm structure but with the optical fiber arranged in a simple circular loop. As shown in Fig. 4(c), the output voltage of the planar dual-spiral structure sensor exhibits a significantly steeper slope as a function of input sound pressure (measured at 1 kHz). The calculated sensitivity reaches 557.82 mV/Pa, representing a remarkable about two times enhancement compared with the 201.61 mV/Pa achieved with the standard single-loop structure under identical conditions. Beyond sensitivity, the intrinsic noise level of the sensor is the other critical factor that determines its ability to detect faint signals. Figure 4(d) presents the measured NEP spectrum for both sensor configurations. The results clearly show that the noise floor of the dual-spiral sensor is significantly lower than that of the conventional single-loop baseline across the entire frequency spectrum. At the standard reference frequency of 1 kHz, the dual-spiral sensor achieves a low NEP of 2.45 $\mathrm{mPa}/\sqrt{\mathrm{Hz}}$, compared with 7.35 $\mathrm{mPa}/\sqrt{\mathrm{Hz}}$ for the single-loop resonator. This low intrinsic noise level is fundamental to achieving the high signal-to-noise ratio detection required for subtle biophysical signals such as BCG. More critically for resolving weak signals embedded in noise, the SNR was substantially improved. Under a 1 kHz signal input, the optical fiber planar dual-spiral resonator achieved an SNR of 24.8 dB, far exceeding the 15.1 dB of the single-loop counterpart, corresponding to a 9.7 dB improvement. This significant SNR enhancement, equivalent to an ∼10-fold increase in the signal power relative to the noise power, drastically improves the system's ability to discern faint physiological details.

Beyond sensitivity and noise metrics, we also characterized the sensor's stability, which is critical for practical deployment. As shown in Fig. 4(e), the sensor maintains robust operation against thermal fluctuations, with signal amplitude variations kept below 5.4% across a temperature range of 25°C to 45°C. Moreover, the long-term reliability is evidenced in Fig. 4(f), where the sensor's sensitivity remained highly consistent over a 4-month period, exhibiting a variation of less than 2.5%. This confirms that the device is free from significant mechanical relaxation or aging effects. These comparative results irrefutably demonstrate the superiority of our proposed optical biophysical sensing unit design incorporating the optical fiber planar dual-spiral resonator and diaphragm coupling. Furthermore, they provide strong experimental support for the pivotal role of the enhanced optomechanical gradient coupling mechanism, facilitated by the planar dual-spiral geometry, in boosting the overall sensing performance, aligning well with our theoretical predictions. The demonstrated high sensitivity, NEP, and SNR are foundational for the successful high-fidelity acquisition and analysis of complex physiological signals presented in the subsequent sections (Figs. 5 and 6).

Although benchmarking against acoustic sensors effectively calibrates the ultimate noise floor of our platform, a more application-relevant comparison is against other state-of-the-art flexible and wearable pressure sensors designed for physiological monitoring. This comparison, however, reveals a fundamental challenge in the field: a lack of standardized reporting for sensitivity and resolution, with units such as V/Pa and $kPa^{-1}$

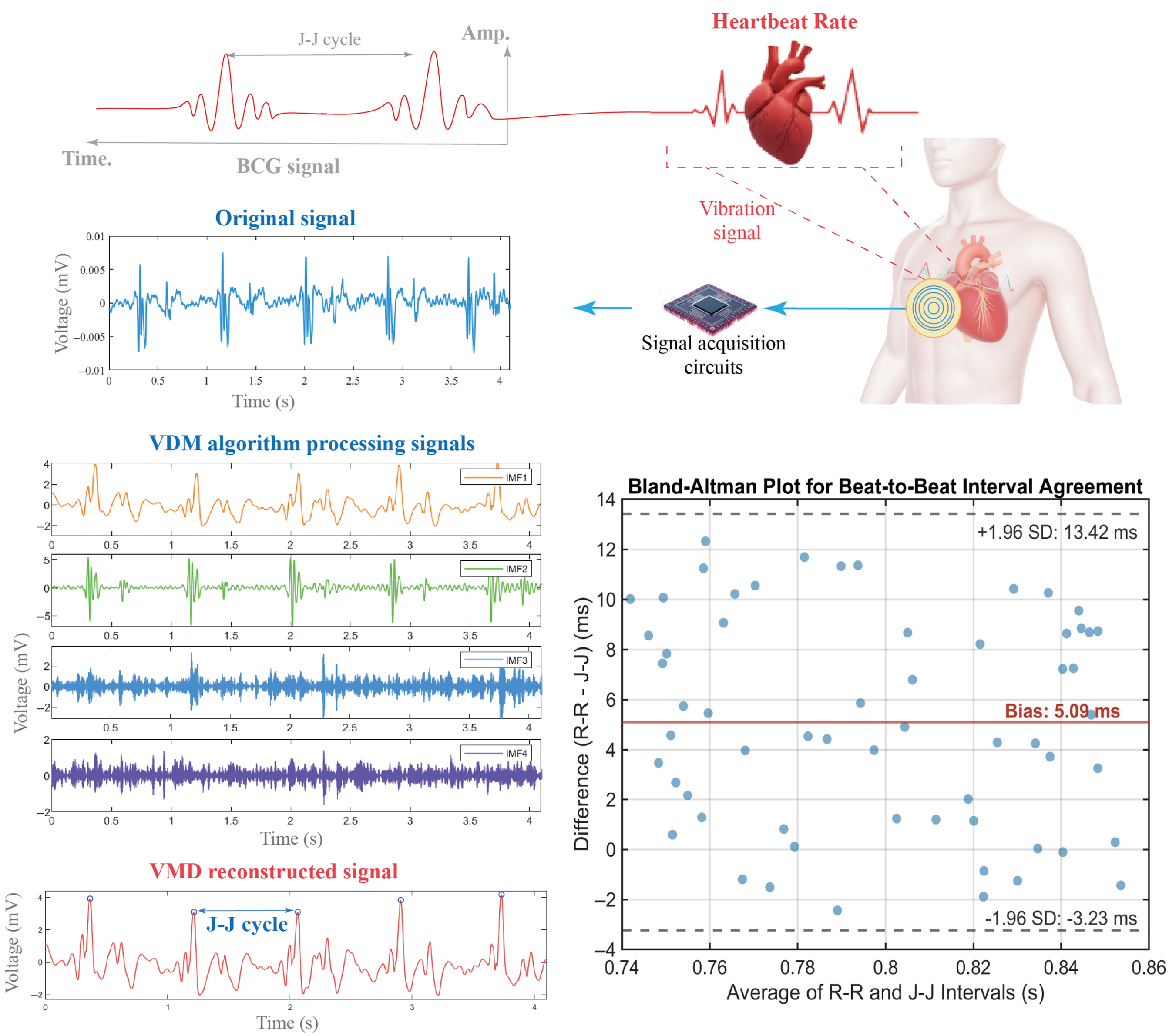


**Fig. 5** BCG signal analysis and gold-standard validation. The signal processing workflow for the BCG signal, illustrating the steps from the original signal, through bandpass filtering and variational mode decomposition (VMD), to the final reconstructed waveform. Moreover, the Bland–Altman plot assesses the agreement between the J-J intervals measured by our sensor and the R-R intervals from a synchronous ECG (gold standard).

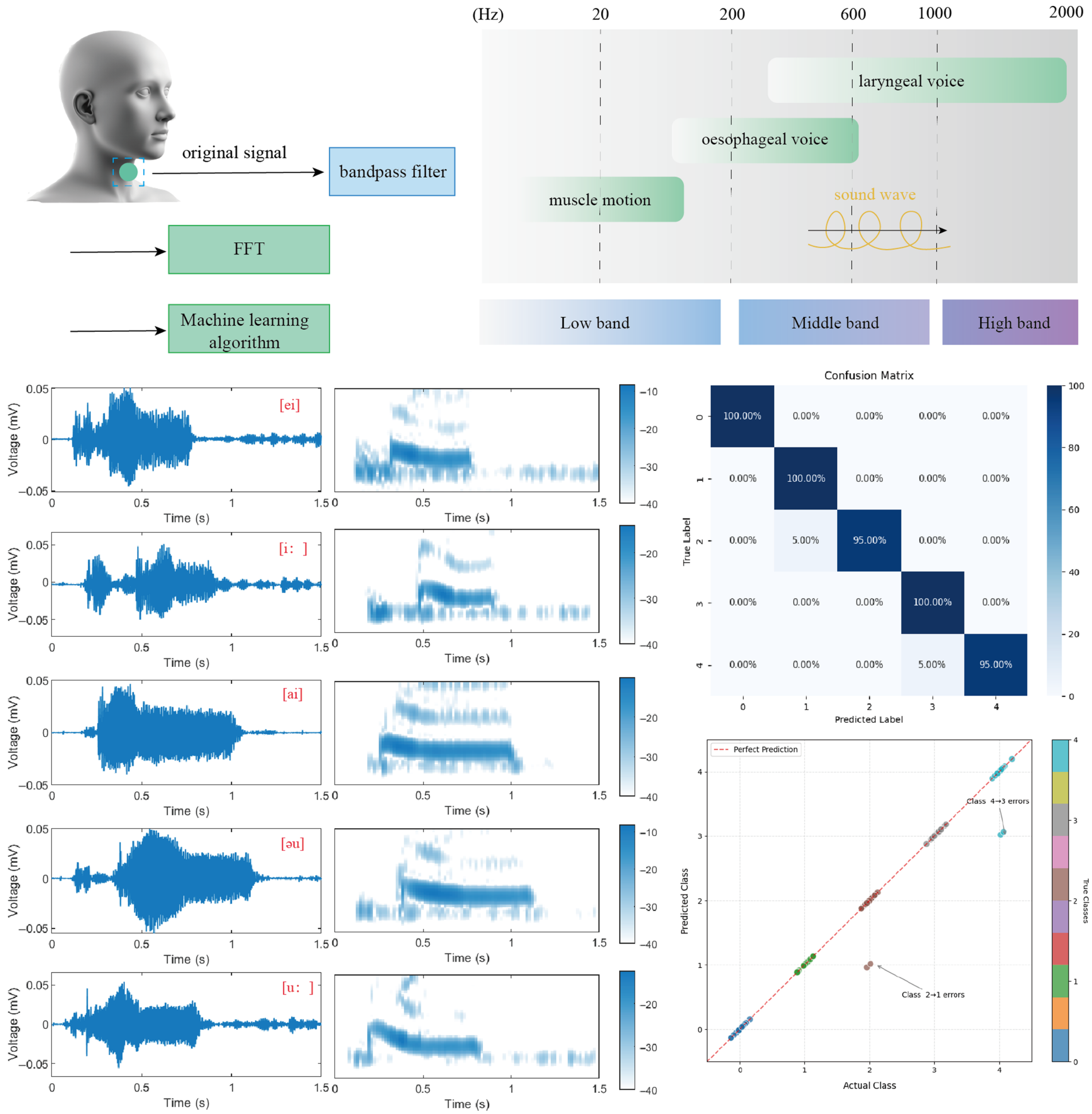


**Fig. 6** High-fidelity vowel acquisition and classification: spectrograms reveal distinct formants enabling >98% recognition accuracy.

describing different physical quantities that are not directly comparable. To overcome this challenge and establish a fair and rigorous comparison, we adopt the NEP, in units of $\mathrm{Pa}/\sqrt{\mathrm{Hz}}$, as the universal golden standard for pressure resolution. For this work, we directly measured the intrinsic NEP of our sensor from its fundamental noise spectrum [as shown in Fig. 3(d)]. For other key works in the literature that do not report NEP directly, we performed a transparent normalization based on their reported minimum detectable pressure ($P_{\min}$) and response time ($\tau$) using the fundamental physical relationship $\mathrm{NEP} \approx P_{\min} \cdot \sqrt{\tau}$. In cases where one of these parameters was not provided, a conservative value was estimated based on the typical reported performance for that specific class of sensor technology to ensure a fair comparison. This process places all sensors onto a common, scientifically robust ground for evaluation.

The results of this standardized benchmarking, summarized in Table 1, unequivocally demonstrate the breakthrough performance of our vectorial optomechanical sensing paradigm. The benchmarking reveals that while sensors based on micro/

**Table 1** Performance benchmarking against state-of-the-art flexible pressure sensors.

| Category | Sensing principle | Ref. | Sensitivity | LOD (Pa) | Response (ms) | NEP ($Pa/\sqrt{Hz}$) | Key features/Trade-offs |
|---|---|---|---|---|---|---|---|
| **Optical sensors (active)** | | | | | | | |
| | Vectorial optomechanics | This work | 557.82 mV/Pa | ~0.14 (est.) | <0.33 | ~$2.45 \times 10^{-3}$ | **Novel Principle**: coherent enhancement; **Fundamental Advantage**: EMI immunity, static pressure capable; **High Performance**: ultra-high resolution |
| | Extrinsic Fabry–Pérot (Passive) | [19] | 33.26 mV/Pa | ~0.003 (est.) | <0.1 | ~$5.89 \times 10^{-5}$ | **Standard Design**: miniature PVC diaphragm structure; **Advantage**: simple passive demodulation; **Trade-off**: fixed sensitivity, lower responsivity than active schemes |
| | Active fiber microcavity (Laser) | [20] | 2600 mV/Pa | ~0.02 (est.) | <0.1 | ~$2.30 \times 10^{-4}$ | **Active Gain**: ultra-high sensitivity via intra-cavity gain; **Advantage**: EMI immunity, wide bandwidth (18 kHz); **Trade-off**: active probe (thermal/gain instability), fixed scalar operation (nontunable) |
| | Evanescent field (MNF) | [21] | 1870 $kPa^{-1}$ | 0.007 | 0.01 | ~$2.2 \times 10^{-5}$ | **Top-tier Resolution**: represents the limit of optical sensing resolution, extremely fast response; **Trade-off**: micro/nanofiber structure can be fragile, complex packaging |
| | Fiber Bragg grating (FBG) | [22] | Varies (e.g., 244 pm/kPa) | ~6000 (est.) | Fast (<1 est.) | ~190 (est.) | **Mature Technology**: EMI immunity, ideal for distributed strain/temp sensing; **Trade-off**: low intrinsic pressure sensitivity, requires special packaging for enhancement |
| **Nonoptical sensors (electronic)** | | | | | | | |
| | Piezoresistive (Graphene/PS) | [23] | 232.5 $kPa^{-1}$ (0–0.2 kPa) | <1 | 45 | ~0.21 (est.) | **Mature Technology**: simple readout; **Trade-off**: susceptible to EMI, temp drift, and material hysteresis; high sensitivity often limited to a narrow pressure range |
| | Piezoresistive (PDMS/Sponge) | [24] | 0.157 $kPa^{-1}$ (0–6 kPa) | ~3 (est.) | ~50 (est.) | ~0.67 (est.) | **High Durability**: >5000 cycles; **Trade-off**: relatively lower sensitivity, also faces EMI and drift issues |
| | Capacitive (MXene) | [25] | 145.5 $kPa^{-1}$ (0–18 kPa) | ~1 (est.) | 68 | ~0.26 (est.) | **High Sensitivity**; **Trade-off**: susceptible to parasitic capacitance and EMI, linearity over a wide range is a challenge |
| | Capacitive (Micro-conformal graphene) | [26] | Up to 7.68 $kPa^{-1}$ | ~1 (est.) | 30 | ~0.17 (est.) | **Extremely High Sensitivity**: can detect very weak forces (1mg); **Trade-off**: same as other capacitive sensors, susceptible to interference |
| **Self-powered sensors** | | | | | | | |
| | Piezoelectric (NW/Graphene) | [27] | $9.4 \times 10^{-3}$ $kPa^{-1}$ | ~1.5 (est.) | 5–7 | ~0.12 (est.) | **Self-powered**: fast response; **Key Advancement**: achieves static pressure measurement via heterojunction; **Trade-off**: relatively low sensitivity, limited resolution |
| | Triboelectric (TENG) (Laminated) | [28] | 7.287 V/kPa | ~24.5 (est.) | ~80 (est.) | ~6.9 (est.) | **Self-powered**: high voltage output, ideal for dynamic event detection; **Fundamental Limitation**: cannot measure static or quasi-static pressure |

The comparison is normalized to the NEP to provide a universal and scientifically rigorous metric for pressure resolution. Note: The limit of detection (LOD) for "This work" is estimated by integrating the measured NEP over the system's full operational bandwidth ($\Delta f = 3$ kHz).

nanofiber (MNF) evanescent fields represent the pinnacle of optical resolution with an NEP two orders of magnitude lower than our device, this extreme performance comes at the cost of significant practical trade-offs, namely the fragility of the micro/nanofiber structure and the complexity of its packaging. Furthermore, a comparative analysis with standard Fabry-Pérot (FP) architectures highlights the strategic advantage of our vectorial approach. As shown in Table 1, conventional passive FP sensors[19] offer compact form factors but suffer from limited sensitivity (33 mV/Pa) due to the lack of optical enhancement. Conversely, active microcavity sensors[20] achieve ultra-high sensitivity (2600 mV/Pa) by introducing gain media, but they are fundamentally limited to "fixed scalar operation." Unlike our system, they cannot tune sensitivity to reject noise. Our sensor strikes a "sweet spot," achieving a high sensitivity of 557.82 mV/Pa—over an order of magnitude higher than passive FP counterparts—on a fully passive, standard-fiber platform and uniquely offering "vectorial tunability" to dynamically optimize the SNR. Beyond the optical domain, this resolution represents a generational leap over mainstream electronic technologies. Our sensor's NEP is four to five orders of magnitude superior to that of leading piezoresistive and capacitive sensors, which, despite claims of high sensitivity, are fundamentally limited by higher intrinsic noise floors and well-known susceptibilities to EMI and material drift. Furthermore, in contrast to self-powered sensors such as triboelectric nanogenerators (TENGs), our vectorial optomechanical approach provides the crucial capability for true static and quasi-static pressure measurement—a function that TENGs cannot perform—in addition to its vastly superior resolution. This unique combination of ultra-high resolution, fundamental EMI immunity, practical robustness, and full-bandwidth (including static) response is the core enabler for the high-fidelity capture of subtle biophysical signals, such as the fine structures in BCG and speech, which lie far beyond the reach of many existing flexible sensor technologies. Beyond the quantitative advantages in NEP, we must emphasize a fundamental qualitative advantage of our optomechanical platform: inherent immunity to EMI. Although the electronic sensors in the benchmark table achieve impressive sensitivities, they are fundamentally susceptible to EMI, which can corrupt faint biophysical signals in real-world settings. Our all-dielectric fiber-based approach eliminates this noise channel, ensuring signal fidelity in complex environments—a key enabling factor for clinical translation.

## 4 Application and System-Level Performance

### 4.1 High-Fidelity Biophysical Signal Monitoring Based on Coherent Dual-Channel Sensing

To demonstrate the capability of our integrated sensing system in practical physiological monitoring scenarios, we applied it to the noninvasive acquisition of BCG signals, which represent the subtle body vibrations generated by cardiac ejection of blood. Capitalizing on the high sensitivity and SNR established in Fig. 4, the sensing unit was placed on the subject's chest to capture these minute mechanical vibrations.

The acquired raw signal underwent a pre-processing pipeline to isolate the signal of interest. Baseline drift was removed by a 4th-order Butterworth bandpass filter (0.8 to 20.0 Hz) to retain the primary frequency content of the BCG signal while rejecting higher frequency noise and irrelevant low-frequency components. Recognizing the complex and often nonstationary nature of BCG signals, which can be coupled with respiratory motion, we employed VMD for further signal decomposition and purification,[29] applying the methodology outlined conceptually in Fig. 3. The VMD algorithm adaptively decomposed the pre-processed signal into a set of intrinsic mode functions (IMFs) (K = 4, $\alpha = 1800$, $\tau = 0.2$) as shown in Fig. 5. The number of modes (K) was set to 4 based on preliminary spectral analysis of the signal, aiming to decompose the signal into its principal components: baseline drift (<0.5 Hz), respiration (0.2 to 0.8 Hz), the cardiac BCG component (0.8 to 20 Hz), and high-frequency noise. The penalty factor ($\alpha$) of 1800 was chosen empirically to ensure adequate spectral separation between these IMFs. Welch's method was performed on each IMF to identify the mode(s) containing the dominant cardiac information, typically exhibiting major frequency components within the expected heart rate range. Subsequently, a high-fidelity BCG waveform was reconstructed by summing the selected cardiac-related IMF components (Fig. 5). Compared with the raw or merely filtered signal, the reconstructed BCG signal exhibits a significantly cleaner and more regular periodic structure, revealing fine morphological details. Using a threshold-based peak detection algorithm applied to the reconstructed signal, key characteristic waves within each cardiac cycle were reliably identified, as marked in Fig. 5. Based on the timing of consecutively detected peaks (J-J intervals), the average heart rate during the recording period was calculated to be 70 bpm. The ability to clearly resolve the fine structures of the BCG waveform, such as the morphology and timing of the I, J, and K waves, underscores the exceptional performance of our optical sensing system combined with advanced signal processing. This demonstrates its capacity to capture and decode complex, low-amplitude physiological vibrations, thereby providing a powerful novel tool for in-depth cardiovascular dynamic analysis and potentially uncovering features missed by conventional measurement techniques. To quantitatively validate the "high fidelity" of the reconstructed BCG signal, we conducted a synchronous comparison study against a gold-standard ECG device. As shown in Fig. 5, the Bland–Altman analysis demonstrates good agreement between our BCG-based measurements and the ECG gold standard, with a mean bias of only 5.09 ms. To quantify the performance, we calculated several key metrics: the mean absolute error (MAE) in beat-to-beat interval determination was only 5.69 ms compared with the R-R intervals from ECG; the J-peak detection sensitivity reached 96.77%, and the positive predictive value (PPV) was 98.31%. These metrics provide strong quantitative evidence that our sensor can capture the cardiac cycle with high accuracy and reliability, thus elevating the claim of "high fidelity" from a subjective description to a rigorously verified scientific fact.

To further demonstrate the versatility and high-fidelity capture capabilities of our optical sensing system, we extended its application to the detection and recognition of human speech signals. The broad operational bandwidth validated in Fig. 4 readily encompasses the primary frequency range of the human voice. This capability is crucial for potential applications in HMI and potentially for monitoring vocal health. In the experiment, subjects vocalized five distinct vowels (/ei/, /i:/, /ai/, /əu/, /u:/) while the sensing unit was placed near the neck. The acquired signals were sampled at 1 kHz. The experiment was conducted with five healthy subjects. Each subject repeated the vocalization for each of the five vowels 30 times, creating a total dataset of 750 samples (5 subjects × 5 vowels × 30 repetitions). This dataset was randomly split into a 70% training set and a 30% testing set. It should be noted that the test was speaker-dependent, meaning data from all subjects were included in both the training and testing sets. Time-frequency analysis was performed using standard short-time Fourier transform (STFT) parameters[30] [32-point Hanning window, 50% overlap, extended fast Fourier transform (FFT) points] to extract spectral features. Representative time-domain waveforms for the five vowels are shown in Fig. 6. Although temporal differences might be subtle, the corresponding frequency spectra clearly reveal the unique acoustic signatures characteristic of each vowel. Specifically, distinct patterns in the location and intensity of spectral peaks, known as formants, are evident for different vowels, providing the critical information for their differentiation. This demonstrates the sensor's ability to capture the fine spectral details inherent in vocal patterns. To quantitatively assess the system's ability to distinguish these subtle vocal features, spectral features were extracted and used to train an LSTM neural network classifier,[31] consistent with the signal processing strategies outlined in Fig. 6. The classification performance is summarized by the confusion matrix presented in Fig. 6. The high values along the diagonal and near-zero off-diagonal elements indicate excellent classification accuracy for all tested vowels. An overall classification accuracy exceeding 98.0% was achieved. This high recognition accuracy strongly validates that our integrated system, combining the high-fidelity optical sensor with appropriate AI-powered signal processing, can effectively capture and decode the complex spectral information embedded within human speech signals. The >98% vowel classification accuracy relies on the high-fidelity capture of distinct formant structures, a capability enabled by the sensor's low noise floor and broad bandwidth. This success in a distinct application domain, following the BCG analysis (Fig. 5), underscores the system's broad applicability and potential for advanced HMI and biomedical voice analysis.

### 4.2 Robustness and Artifact-Resilient Operation under Dynamic Conditions

The transition of a precision biophysical sensing technology from the laboratory to real-world applications hinges on its robustness in dynamic environments. This section systematically discusses the multi-layered strategy employed in this work to ensure the reliability of the measurements, addressing two primary challenges: (1) internal polarization state instability caused by environmental perturbations and (2) external motion artifacts arising from the user's physical activities. Strategy for Polarization Stability: The performance of the frequency-polarization coupling enhancement mechanism is highly dependent on a controllable static polarization bias angle, $\theta_0$. To ensure the stability of this operating point, a comprehensive solution was adopted. At the material level, the high-birefringence polarization-maintaining (PM) fiber that constitutes the resonator provides a powerful, fundamental polarization stability, robust against weak, random external stress perturbations. At the structural level, the localized sensing design ensures efficient coupling for the target signal while physically isolating non-target disturbances. Most importantly, at the strategic level of operating point selection, an active trade-off can be made between performance and stability. Both theory and experiment (Fig. 3) indicate that it is not necessary to set the operating point at the theoretical peak, $\theta_{0,\max}$, where the sensitivity is highest but also the steepest. In practice, a "robust operating zone" can be strategically chosen, where the sensitivity is still sufficiently high (e.g., 90% of the peak value) but the response curve is relatively flat. This approach significantly enhances system stability at the cost of a minor sacrifice in ultimate performance. Single-channel motion artifact suppression strategy: for the inevitable motion artifacts in wearable applications, this work proposes an intelligent suppression scheme based entirely on single-channel optical signal processing. The core of this scheme is that the target physiological signal (e.g., BCG) and motion artifacts exhibit significant differences in their temporal morphology and oscillatory characteristics, even when their frequency bands overlap. First, in the pre-processing stage, high-energy transient spikes characteristic of severe motion can be identified via amplitude thresholding and excluded from analysis. Second, and most critically, the VMD algorithm is utilized for adaptive signal separation. VMD decomposes the mixed signal into a series of IMFs, each with distinct oscillatory properties. Typically, the BCG signal, which is strictly synchronized with the cardiac cycle, is concentrated in one or a few specific IMFs, whereas high-energy, often non-periodic artifacts associated with body movements are partitioned into other IMFs. By analyzing the energy, frequency, and rhythmicity of each IMF, the modes dominated by motion artifacts can be intelligently identified and discarded. Only the IMFs representing the true physiological signal are then reconstructed. This signal separation in the modal domain enables the efficient extraction of high-fidelity physiological information from a single, contaminated data stream without relying on any additional sensors. In summary, although an ultra-high stability sensor for clinical-grade applications might ultimately require physical designs like a dual-cavity differential system, this work demonstrates that a combination of intrinsic material properties, judicious structural design, intelligent operating point selection, and advanced single-channel signal decomposition algorithms provides the necessary feasibility and robustness for the current architecture to perform high-fidelity biophysical dynamic measurements.

## 5 Conclusion

In conclusion, this work has conducted an in-depth investigation and demonstrated the control of the coherent coupling process between orthogonal frequency and polarization modes within an engineered optomechanical resonator. We have successfully answered a key physical question: through sophisticated device architecture, polarization "noise" can indeed be transformed into a coherent "channel" that is actively and precisely controllable and can be utilized to overcome the limits of conventional sensing. We have proposed and demonstrated a novel paradigm of "vectorial optomechanical sensing" based on an engineered optomechanical resonator. By designing an innovative planar dual-spiral resonator and combining it with a key experimental validation, we have shown that a single mechanical strain can be synchronously and efficiently transduced onto two orthogonal degrees of freedom of light. Our physical model accurately predicted the coherent superposition behavior of these channels, a core mechanism that was unequivocally validated by our systematic measurements of the total sensitivity as a function of the static polarization bias angle, confirming the accuracy of the theory and the effectiveness of the structural design. Ultimately, the sensor achieved a high sensitivity of 557.82 mV/Pa, a low noise level of 2.45 $\mathrm{mPa}/\sqrt{\mathrm{Hz}}$, and a high SNR of 24.8 dB, demonstrating its outstanding performance in the high-fidelity monitoring of biophysical signals. Crucially, the successful realization of a 3 kHz sensing bandwidth under PDH interrogation overcomes the typical low-frequency limitation of such systems, directly enabling the high-fidelity monitoring of dynamic biophysical signals. Finally, we address the system integration aspect. Although the proposed sensor head features ideal wearable characteristics—being lightweight, flexible, and electromagnetic-interference-free—the current interrogation relies on benchtop PDH instrumentation to ensure maximum signal fidelity for physical validation. Transitioning from a "wearable probe" to a "fully wearable system" is a clear engineering roadmap. Recent advancements in photonic integrated circuits (PICs) have successfully demonstrated chip-scale tunable lasers and on-chip feedback loops. Leveraging these technologies, future iterations of this platform can integrate the bulky readout unit into a compact, battery-powered module, thereby unlocking its full potential for ubiquitous clinical applications. More than just providing a novel strategy for high-sensitivity sensing, this work establishes a novel paradigm of "vectorial optomechanical sensing," extending the field from conventional scalar frequency sensing to the active utilization of the vectorial properties of the light field. This principle of actively controlling the coherent interplay between orthogonal modes through structural engineering offers a universal pathway. We believe this principle can be generalized to various other high-$Q$ resonant platforms, such as silicon-based microrings and photonic crystal cavities, opening up exciting novel directions for surpassing their conventional sensing limits and exploring richer physical phenomena.[32,33]

## Disclosures

The authors declare no conflicts of interest.

## Code and Data Availability

Data underlying the results presented in this paper are not publicly available at this time but may be obtained from the authors upon reasonable request.

### Acknowledgments

This work was supported by the National Natural Science Foundation of China (Grant No. 62405027), the Guangdong Basic and Applied Basic Research Foundation (Grant No. 2025A1515010176), the Scientific Research Project of Liaoning Provincial Education Department (Grant No. LJKMZ 20220544), and the Fonds de la Recherche Scientifique (F.R.S.-FNRS) under the Postdoctoral Researcher grant (Chargé de Recherches) of Xuehao Hu.

### References

1. Y. Yu et al., "Technologies for non-invasive physiological sensing: Status, challenges, and future horizons," *Biosens. Bioelectron.: X* **16**, 100420 (2024).
2. S. C. Mukhopadhyay, "Wearable sensors for human activity monitoring: a review," *IEEE Sens. J.* **15**(3), 1321–1330 (2014).
3. M. Maimaiti, H. Zhu, and H. Zeng, "Applications of ballistocardiogram in the diagnosis of coronary heart disease: systematic review," *JMIR Cardiol.* **9**, e68197 (2025).
4. K. Remesh and J. Chunkath, "Comparison of HRV indices of ECG and BCG signals," arXiv:2307.08960 (2023).
5. G. Fagherazzi et al., "Voice for health: the use of vocal biomarkers from research to clinical practice," *Digit. Biomark.* **5**(1), 78–88 (2021).
6. C. Chircov and A. M. Grumezescu, "Microelectromechanical systems (MEMS) for biomedical applications," *Micromachines* **13**(2), 164 (2022).
7. M. Sharma and A. Kumar, "A review on piezo-and pyroelectric responses of flexible nano-and micropatterned polymer surfaces for biomedical sensing and energy harvesting applications," *Nano Energy* **80**, 105527 (2021).
8. W. Li et al., "Wearable photonic smart wristband for cardiorespiratory function assessment and biometric identification," *Opto-Electron. Adv.* **8**(5), 240254 (2025).
9. M. A. Butt, "Beyond the detection limit: a review of high-q optical ring resonator sensors," *Mater. Today Phys.* **58**, 101873 (2025).
10. X. Liu et al., "Progress of optomechanical micro/nano sensors: a review," *Int. J. Optomechatron.* **15**(1), 120–159 (2021).
11. H. Wang et al., "Optical tactile sensor based on a flexible optical fiber ring resonator for intelligent Braille recognition," *Opt. Express* **33**, 2512–2528 (2025).
12. P. Roriz et al., "Review of fiber-optic pressure sensors for biomedical and biomechanical applications," *J. Biomed. Opt.* **18**(5), 050903 (2013).
13. Z. Wang et al., "Recent advancements in resonant fiber optic gyro–a review," *IEEE Sens. J.* **22**(19), 18240–18252 (2022).
14. R. Ulrich and M. Johnson, "Fiber-ring interferometer: polarization analysis," *Opt. Lett.* **4**(5), 152–154 (1979).
15. H. Ma et al., "Polarization-induced noise in resonator fiber optic gyro," *Appl. Opt.* **51**(28), 6708–6717 (2012).
16. Z. Jiang et al., "Sensitivity and noise analysis of resonant all-fiber optic current transformers," *IEEE Photonics J.* **16**(4), 1–8 (2024).
17. R. W. P. Drever et al., "Laser phase and frequency stabilization using an optical resonator," *Appl. Phys. B* **31**(2), 97–105 (1983).
18. E. D. Black, "An introduction to Pound-Drever-Hall laser frequency stabilization," *Amer. J. Phys.* **69**, 79 (2001).
19. Q. Yao et al., "A miniature Fabry–Pérot fiber interference sensor based on polyvinyl chloride membrane for acoustic pressure sensing in mid–high-frequency band," *Materials* **14**(24), 7605 (2021).
20. X.-X. Gao et al., "An acoustic sensor based on active fiber Fabry–Pérot microcavities," *Sensors* **20**(20), 5760 (2020).
21. W. Yu et al., "Highly sensitive and fast response strain sensor based on evanescently coupled micro/nanofibers," *Opto-Electron. Adv.* **5**(9), 210101 (2022).
22. S. Xu et al., "Fiber Bragg grating pressure sensors: a review," *Opt. Eng.* **62**(1), 010902 (2023).
23. R. Li et al., "Graphene-based, flexible, wearable piezoresistive sensors with high sensitivity for tiny pressure detection," *Sensors* **25**(2), 423 (2025).
24. Q. Zhang et al., "Flexible piezoresistive sensor with high stability based on GO@PDMS-PU porous structure," *Symmetry* **17**(5), 773 (2024).
25. L. Zhang et al., "Highly sensitive capacitive flexible pressure sensor based on a high-permittivity MXene nanocomposite and 3D network electrode for wearable electronics," *ACS Sens.* **6**(7), 2630–2641 (2021).
26. J. Yang et al., "Flexible, tunable, and ultrasensitive capacitive pressure sensor with microconformal graphene electrodes," *ACS Appl. Mater. Interfaces* **11**(14), 13491–13498 (2019).
27. Z. Chen et al., "Flexible piezoelectric-induced pressure sensors for static measurements based on nanowires/graphene heterostructures," *ACS Nano* **11**(5), 4507–4513 (2017).
28. A. A. Jan, S. Kim, and S. Kim, "A skin-wearable and self-powered laminated pressure sensor based on triboelectric nanogenerator for monitoring human motion," *Soft Sci.* **4**, 10 (2024).
29. K. Dragomiretskiy and D. Zosso, "Variational mode decomposition," *IEEE Trans. Signal Process.* **62**(3), 531–544 (2014).
30. A. V. Oppenheim and R. W. Schafer, *Discrete-Time Signal Processing*, 3rd ed., Pearson (2009).

31. S. Hochreiter and J. Schmidhuber, "Long short-term memory," *Neural Computat.* **9**(8), 1735–1780 (1997).
32. W. Bogaerts et al., "Silicon microring resonators," *Laser Photonics Rev.* **6**(1), 47–73 (2012).
33. J. Xia et al., "Opto-mechanical photonic crystal cavities for sensing application," *Appl. Sci.* **10**(20), 7080 (2020).

**Rui Min** received his PhD from the Universidad Politécnica de Valencia, Valencia, Spain, in 2019. Now, he is an associate professor with the Faculty of Arts and Sciences, Beijing Normal University, Beijing, China. He has authored or coauthored more than 180 articles and conference papers with 4500 citations (H-index: 36). His current research interests include wearable devices and brain interface. He is also an Associate Editor of *Optics Express*, *IEEE Sensors Journal*, and *Frontiers in Physics*.

**Zhuo Wang** received his PhD from Harbin Institute of Technology, Harbin, China, in 2022. He is currently an assistant professor with the Department of Physics, Beijing Normal University, China. To date, he has authored or coauthored over 60 articles and conference papers. His primary research interests include precision optical sensing architectures and flexible fiber-optic sensors, alongside their applications in high-fidelity physiological monitoring, optical nervous systems, and embodied intelligence.

Biographies of the other authors are not available.